The LES Code: Description & Validation Studies

Section 1 contains a detailed description of the equations and of numerical algorithms implemented in the code for solving these equations. Section 2 contains the results of a number of validation studies including temporal and spatial convergence rates, the effects of grid cell size and the sub-grid closure, and the overall accuracy of the code in simulating decaying isotropic turbulence and turbulent channel flow.

1 Formulation

Application of a homogeneous, low-pass spatial filter to the non-dimensionalized C-L equations leads to

$$\begin{aligned} \frac{\partial \bar{u}_i}{\partial x_i} &= 0 \\ \frac{\partial \bar{u}_i}{\partial t} + \bar{u}_j \frac{\partial \bar{u}_i}{\partial x_j} &= -\frac{\partial \bar{\Pi}}{\partial x_i} + \frac{1}{\mathrm{Re}} \frac{\partial^2 \bar{u}_i}{\partial x_j^2} + \frac{\partial \tau_{ij}}{\partial x_j} + \frac{1}{\mathrm{La}_t^2} \epsilon_{ijk} \phi_j^s \bar{\omega}_k + F_i \end{aligned} \tag{1}$$

where ϵ_{ijk} is the totally antisymmetric third rank tensor, an over-bar denotes application of the low-pass spatial filter and $\bar{u}_i$ and $\bar{\omega}_i$ are the i-th components of the non-dimensional space and time filtered velocity and vorticity, respectively, in the Cartesian coordinate system (x_1, x_2, x_3). Recall that the C-L equations govern the behavior of time filtered variables. Furthermore, the C-L equations were spatially filtered, leading to the equations in (1); hence, $\bar{u}_i$ and $\bar{\omega}_i$ are referred to as the *space and time filtered* velocity and vorticity, respectively. The non-dimensional, modified, space and time filtered pressure is defined as

$$\bar{\Pi} = \bar{p} + \frac{1}{2}\Gamma, \tag{2}$$

where $\bar{p}$ is the non-dimensional, space and time filtered pressure and

$$\Gamma = \frac{1}{\mathrm{La}_t^4} \phi_i^s \phi_i^s + \frac{2}{\mathrm{La}_t^2} \bar{u}_i \phi_i^s. \tag{3}$$

The fourth (next to last) term on the right hand side of the second equation in (1) is the non-dimensionalized C-L vortex force defined as the Stokes drift velocity crossed with the filtered vorticity. The non-dimensional Stokes drift velocity is defined by Phillips (1967) and LeBlond and Mysak (1978) as

$$\phi_1^s = \frac{\cosh(2\kappa x_3)}{2\sinh^2(\kappa H)} \quad \text{and} \quad \phi_2^s = \phi_3^s = 0, \tag{4}$$

where H is the water depth and κ is the dominant wavenumber of the filtered-out surface gravity waves. F_i is the ith component of a body force.

The characteristic flow velocity is taken as the friction velocity, u_τ, where $u_\tau = (\tau_\mathrm{s}/\rho_o)^{1/2}$, τ_s is the constant wind stress in the x_1-direction applied at the top surface and

ρ_o is the constant density. Non-dimensionalizing the governing equations with characteristic flow velocity u_τ and characteristic length scale $\delta = H/2$ gives rise to the turbulent Langmuir number, $\mathrm{La}_t = (u_\tau/u_s)^{1/2}$, and the Reynolds number $\mathrm{Re} = u_\tau \delta/\nu$ (with ν the kinematic viscosity) appearing in (1). The characteristic Stokes drift velocity is defined as $u_s = \omega k a^2$, where ω is the dominant frequency, κ is the dominant wavenumber and a is the amplitude of the surface gravity waves.

1.1 Subgrid-scale closure

The subgrid-scale (SGS) stress τ_{ij} in (1), generated by spatial filtering the C-L equations, is defined as

$$\tau_{ij} = \bar{u}_i \bar{u}_j - \overline{u_i u}_j. \tag{5}$$

The term $\overline{u_i u}_j$ gives rise to a closure problem and thus must be parameterized. The deviatoric part of τ_{ij} (i.e. $\tau^d_{ij} \equiv \tau_{ij} - \delta_{ij}\tau_{kk}/3$) is parameterized using the dynamic Smagorinsky closure and the dilatational part (i.e. $\delta_{ij}\tau_{kk}/3$) is added to the modified pressure, $\bar{\Pi}$. The Smagorinsky closure expresses the deviatoric part of the SGS stress as

$$\tau^d_{ij} = 2 \underbrace{(C_s \bar{\Delta})^2 |\bar{S}|}_{\text{eddy viscosity}} \bar{S}_{ij}, \tag{6}$$

where $\bar{\Delta}$ is the width of the grid filter (i.e. the smallest characteristic length scale resolved by the discretization), C_s is the Smagorinsky coefficient, $\bar{S}_{ij} = (\bar{u}_{i,j} + \bar{u}_{j,i})/2$ is the filtered strain-rate tensor, and $|\bar{S}| = (2\bar{S}_{ij}\bar{S}_{ij})^{1/2}$ is its norm. The model coefficient is computed dynamically (Lilly, 1992) as

$$(C_s \bar{\Delta})^2 = \frac{1}{2} \frac{\langle L_{ij} M_{ij} \rangle}{\langle M_{kl} M_{kl} \rangle}, \tag{7}$$

where

$$L_{ij} = \widetilde{\bar{u}_i \bar{u}_j} - \tilde{\bar{u}}_i \tilde{\bar{u}}_j, \tag{8}$$

and

$$M_{ij} = \widetilde{|\bar{S}| \bar{S}}_{ij} - \alpha^2 |\tilde{\bar{S}}| \tilde{\bar{S}}_{ij}. \tag{9}$$

An over-tilde, $\tilde{\cdot}$, denotes application of a homogeneous, low-pass, spatial test filter in the x_1 and x_2 directions. Angle brackets in (7) denote averaging in x_1 and x_2 as means of preventing instabilities due to potential negative values of the model coefficient. Finally, α is a parameter referred to as the filter width ratio and often approximated as the test filter width divided by the grid cell size, h. All of the simulations described here were performed using the well-known box filter of width $2h$ (Pope, 2000) approximated using the trapezoidal rule. The width of the resulting discrete filter is $\sqrt{6}h$ (Lund, 1997), thus $\alpha = \sqrt{6}$.

In addition to the dynamic Smagorinsky closure, test runs using the closure of Morinishi and Vasilyev (2001) were carried out to determine whether or not the results were sensitive to the sub-grid scale closure. In the latter closure, the deviatoric part of the SGS stress is computed as

$$\tau^d_{ij} = C_L (\bar{\bar{u}}_i \bar{\bar{u}}_j - \overline{\bar{u}_i \bar{u}}_j)^d + 2(C_s \bar{\Delta})^2 |\bar{S}| \bar{S}_{ij}. \tag{10}$$

In the former closure, τ_{ij}^d is given by (6). The coefficient $(C_s\bar{\Delta})^2$ in (40) is computed dynamically in the same way as before in (7). The coefficient C_L is computed dynamically as

$$C_L = \frac{\left\langle [L_{ij} + 2(C_s\bar{\Delta})^2 M_{ij}] H_{ij}^d \right\rangle}{\left\langle H_{kl}^d H_{kl}^d \right\rangle}, \tag{11}$$

where L_{ij} and M_{ij} are specified in (8) and (9), respectively, and

$$H_{ij} = (\widehat{\bar{\hat{u}}_i \bar{\hat{u}}_j} - \bar{\hat{\bar{u}}}_i \bar{\hat{\bar{u}}}_j) - (\widehat{\bar{u}_i \bar{u}_j} - \bar{\hat{\bar{u}}}_i \bar{\hat{\bar{u}}}_j). \tag{12}$$

Recall that the hat notation $\hat{\cdot}$, denotes application of a test filter over the horizontal directions of the flow. The bar notation, $\bar{\cdot}$, denotes application of the grid filter, implicitly set by the numerical method. Knowledge of the grid filter or at least an approximation to the grid filter is needed in order to compute the tensor H_{ij}. As an approximation to grid filtering, the following operation suggested by Morinishi and Vasilyev is used:

$$\bar{f}(x_i^*) = \frac{1}{24}[f(x_i^* - h_i) + 22 f(x_i^*) + f(x_i^* + h_i)], \tag{13}$$

where $\bar{f}(x_i^*)$ is function f filtered over the x_i-direction evaluated at $x_i = x_i^*$ and h_i is the grid cell size in the x_i-direction. The width characterizing the filter induced by the operation in (43) is $\bar{\Delta}_i = h_i$. In the current implementation, the filter operation in (43) was applied over periodic directions of the flow (x_1 and x_2).

1.2 Temporal discretization

The continuity and momentum equations in (1) are solved on a non-staggered grid using the second order time accurate semi-implicit fractional step method analyzed by Armfield and Street (2000). Fractional-step methods integrate the equations in (1) in a segregated manner. In other words, the momentum equations are first solved for the velocity and some form of Poisson's equation is solved for pressure. The Poisson's equation is derived using the continuity and momentum equations. Thus, solution of this equation provides the pressure and also acts to enforce continuity.

For simplicity, the advection, gradient of the subgrid-scale stress, the C-L vortex force, and the forcing terms are gathered into function H_i as

$$H_i(\bar{u}_k) = \bar{u}_j \frac{\partial \bar{u}_i}{\partial x_j} - \frac{\partial \tau_{ij}^d}{\partial x_j} - \epsilon_{ijk} \frac{1}{\mathrm{La}_t^2} \phi_j^s \bar{\omega}_k - F_i. \tag{14}$$

Reverting to vector notation (i.e. $\bar{\mathbf{u}} = (\bar{u}_1, \bar{u}_2, \bar{u}_3)$, $\nabla = (\partial_{x_1}, \partial_{x_2}, \partial_{x_3})$, $\mathbf{H} = (H_1, H_2, H_3)$ and so on) the terms in (14) are explicitly discretized using the second-order time accurate Adams-Bashforth scheme as

$$\mathbf{N}(\bar{\mathbf{u}}^n, \bar{\mathbf{u}}^{n-1}) = \frac{3}{2}\mathbf{H}(\bar{\mathbf{u}}^n) - \frac{1}{2}\mathbf{H}(\bar{\mathbf{u}}^{n-1}), \tag{15}$$

where the superscripts refer to time steps n and $n-1$. Using the second order time accurate Crank-Nicholson scheme to discretize the viscous term together with the previous

Adams-Bashforth scheme, the discretized momentum equation may be re-expressed as

$$\begin{aligned}
\left(\frac{1}{\Delta t}-\frac{1}{2\mathrm{Re}}\nabla^2\right)\Delta\bar{\mathbf{u}}_*^{n+1} &= -N(\bar{\mathbf{u}}^n,\bar{\mathbf{u}}^{n-1})+\frac{1}{\mathrm{Re}}\nabla^2\bar{\mathbf{u}}^n-\nabla\bar{\Pi}^n \quad \text{in } \Omega \\
\mathbf{t}_i\cdot\bar{\mathbf{u}}_*^{n+1} &= 0 \quad \text{for } i=1,2 \quad \text{on } \partial\Omega_1 \\
(\mathbf{n}\cdot\nabla)(\bar{u}_{1*}^{n+1},\bar{u}_{2*}^{n+1}) &= (\mathrm{Re},0) \quad \text{on } \partial\Omega_2 \\
\bar{\mathbf{u}}_*^{n+1} &= \bar{\mathbf{u}}^n+\Delta\bar{\mathbf{u}}_*^{n+1} \quad \text{in } \Omega+\partial\Omega,
\end{aligned} \tag{16}$$

where $\bar{\mathbf{u}}_*^{n+1}=(\bar{u}_{1*}^{n+1},\bar{u}_{2*}^{n+1},\bar{u}_{3*}^{n+1})$, Δt is the time step, $\mathbf{n}$ is the unit normal vector to either the bottom or top boundary, $\partial\Omega_1$ denotes the bottom boundary and $\partial\Omega_2$ denotes the top boundary. Furthermore, Ω denotes the interior of the domain excluding the boundaries and $\partial\Omega$ denotes both bottom and top boundaries. Vectors $\mathbf{t}_1$ and $\mathbf{t}_2$ are linearly independent unit vectors normal to $\mathbf{n}$. The solution of (16) at time t_{n+1}, intermediate solution $\bar{\mathbf{u}}_*^{n+1}$, does not satisfy the continuity equation. To enforce the diverge-free condition, the following Poisson's equation for pressure is firstly solved:

$$\begin{aligned}
\nabla^2(\Delta\bar{\Pi}^{n+1}) &= \frac{1}{\Delta t}\,\nabla\cdot\bar{\mathbf{u}}_*^{n+1} \quad \text{in } \Omega+\partial\Omega \\
\frac{\partial\Delta\bar{\Pi}^{n+1}}{\partial\mathbf{n}} &= \frac{1}{\Delta t}\,\mathbf{n}\cdot\bar{\mathbf{u}}_*^{n+1} \quad \text{on } \partial\Omega \\
\bar{\Pi}^{n+1} &= \bar{\Pi}^n+\Delta\bar{\Pi}^{n+1} \quad \text{in } \Omega+\partial\Omega.
\end{aligned} \tag{17}$$

The divergence-free velocity is finally obtained as

$$\bar{\mathbf{u}}^{n+1}=\bar{\mathbf{u}}_*^{n+1}-\Delta t\,\nabla(\Delta\bar{\Pi}^{n+1}) \quad \text{in } \Omega+\partial\Omega. \tag{18}$$

Notice that in the second equation in (16), the component of the intermediate velocity normal to the bottom and top boundaries (i.e. $\mathbf{n}\cdot\bar{\mathbf{u}}_*^{n+1}=\bar{u}_{3*}^{n+1}$ on $\partial\Omega$) is not specified and thus kept free as given by the solution of the first equation in (16). In turn, this free velocity affects the solution of the Poisson's equation for pressure through the boundary condition in (17). As discussed by Slinn and Riley (1998), this is required to ensure convergence of the method. However, at the end of the time step, when the final velocity is computed via (18), $\bar{u}_3^{n+1}$ is set to zero on $\partial\Omega$, thus satisfying the true boundary condition.

1.3 Spatial discretization

The spatial discretization is hybrid, as it makes use of fast Fourier transforms in the horizontal direction (x_1 and x_2) and high order finite differences in the vertical direction (x_3). Taking the two-dimensional Fourier transform of the temporally discrete momentum equation in (16) and denoting a Fourier transformed quantity with an over-hat, $\hat{\cdot}$, leads

to

$$\begin{aligned}
\left(\frac{1}{\Delta t}+\frac{1}{2\mathrm{Re}}|\mathbf{k}_h|^2-\frac{1}{2\mathrm{Re}}\frac{\delta^2}{\delta x_3^2}\right)\widehat{\Delta\bar{\mathbf{u}}}_*^{n+1} &= -\hat{N}(\bar{\mathbf{u}}^n,\bar{\mathbf{u}}^{n-1})-\nabla_s\,\hat{\bar{\Pi}}^n \\
&\quad +\frac{1}{\mathrm{Re}}\left\{-|\mathbf{k}_h|^2+\frac{\delta^2}{\delta x_3^2}\right\}\hat{\bar{\mathbf{u}}}^n \quad \text{in } \Omega \\
\left(\hat{\bar{u}}_{1*}^{n+1},\hat{\bar{u}}_{2*}^{n+1}\right) &= (0,0) \quad \text{on } \partial\Omega_1 \\
\left(\frac{\delta\hat{\bar{u}}_{1*}^{n+1}}{\delta x_3},\frac{\delta\hat{\bar{u}}_{2*}^{n+1}}{\delta x_3}\right) &= (\mathrm{Re},0) \quad \text{on } \partial\Omega_2 \\
\hat{\bar{\mathbf{u}}}_*^{n+1} &= \hat{\bar{\mathbf{u}}}^n+\widehat{\Delta\bar{\mathbf{u}}}_*^{n+1} \quad \text{in } \Omega,
\end{aligned} \tag{19}$$

where $\mathbf{k}_h = k_1\mathbf{e}_1 + k_2\mathbf{e}_2$ and k_1 (*viz.* $\mathbf{e}_1$) and k_2 (*viz.* $\mathbf{e}_2$) are the wavenumbers (*viz.* unit vectors) in the x_1 and x_2 directions, respectively. The operator $\delta/\delta x_3$ denotes the finite difference approximation of $\partial/\partial x_3$ and $\nabla_s = (ik_1, ik_2, \delta/\delta x_3)$; these are shown in the finite-difference stencils section below.

Taking the two-dimensional Fourier transport of the Poisson's equation in (17) leads to

$$\begin{aligned}
\left(-|\mathbf{k}_h|^2+\frac{\delta^2}{\delta x_3^2}\right)\widehat{\Delta\bar{\Pi}}^{n+1} &= \frac{1}{\Delta t}\left(ik_1\hat{\bar{u}}_{1*}^{n+1}+ik_2\hat{\bar{u}}_{2*}^{n+1}+\frac{\delta}{\delta x_3}\hat{\bar{u}}_{3*}^{n+1}\right) \quad \text{in } \Omega+\partial\Omega \\
\frac{\delta\widehat{\Delta\bar{\Pi}}^{n+1}}{\delta x_3} &= \frac{1}{\Delta t}\hat{\bar{u}}_{3*}^{n+1} \quad \text{on } \partial\Omega \\
\hat{\bar{\Pi}}^{n+1} &= \hat{\bar{\Pi}}^n+\widehat{\Delta\bar{\Pi}}^{n+1} \quad \text{in } \Omega+\partial\Omega.
\end{aligned} \tag{20}$$

The velocity at time step $n+1$ becomes

$$\begin{aligned}
\hat{\bar{u}}_1^{n+1} &= \hat{\bar{u}}_{1*}^{n+1}-i\,\Delta t\,k_1\widehat{\Delta\bar{\Pi}}^{n+1} \quad \text{in } \Omega+\partial\Omega \\
\hat{\bar{u}}_2^{n+1} &= \hat{\bar{u}}_{2*}^{n+1}-i\,\Delta t\,k_2\widehat{\Delta\bar{\Pi}}^{n+1} \quad \text{in } \Omega+\partial\Omega \\
\hat{\bar{u}}_3^{n+1} &= \hat{\bar{u}}_{3*}^{n+1}-\Delta t\frac{\delta}{\delta x_3}\widehat{\Delta\bar{\Pi}}^{n+1} \quad \text{in } \Omega+\partial\Omega.
\end{aligned} \tag{21}$$

The reader is reminded that at the end of the time step, after the final velocity is computed via (21), $\hat{\bar{u}}_3^{n+1}$ is set to zero on $\partial\Omega$ (the bottom and top boundaries). This is also done for $\hat{\bar{u}}_1^{n+1}$ and $\hat{\bar{u}}_2^{n+1}$ on $\partial\Omega_1$ (the bottom boundary).

1.4 Finite difference stencils

Using compact finite difference schemes, second and first order derivatives of function $f(z)$ on $[a,b]$ are obtained. Consider the set $\{z_1, z_2, z_3, \cdots, z_N, z_{N+1}\}$ of equi-distant

points gridding the interval $[a, b]$ with h being the distance between the points. The second and first derivatives of $f(z)$ may be obtained from

$$\mathbf{A}\ \mathbf{f}'' = \mathbf{B}\ \mathbf{f} \quad \text{thus} \quad \mathbf{f}'' = \left\{\mathbf{A}^{-1}\mathbf{B}\right\}\ \mathbf{f} \tag{22}$$

and

$$\mathbf{C}\ \mathbf{f}' = \mathbf{D}\ \mathbf{f} \quad \text{thus} \quad \mathbf{f}' = \left\{\mathbf{C}^{-1}\mathbf{D}\right\}\ \mathbf{f} \tag{23}$$

where $\mathbf{f} = (f_1, f_2, \cdots, f_N)^t$ and f_i is $f(z)$ evaluated at $z_i \in [a, b]$. Matrices $\mathbf{A}$, $\mathbf{B}$, $\mathbf{C}$, and $\mathbf{D}$ are banded. However, matrices $\mathbf{A}^{-1}\mathbf{B}$ and $\mathbf{C}^{-1}\mathbf{D}$ are full. Next, the stencils used to generate these matrices are detailed.

1.4.1 First order derivative

Let f_i' denote the first derivative of $f(z)$ at $z = z_i$. For $i > 2$ and $i < N$, the first derivative of function $f(z)$ is approximated via

$$\frac{1}{3}f'_{i-1} + f'_i + \frac{1}{3}f'_{i+1} = \frac{1}{h}\left(-\frac{1}{36}f_{i-2} - \frac{7}{9}f_{i-1} + \frac{7}{9}f_{i+1} + \frac{1}{36}f_{i+2}\right). \tag{24}$$

Detailed analysis of this $O(h^6)$ approximation is given by Lele (1992). For $i = 1$, the first derivative may be obtained from the following $O(h^5)$ approximation:

$$f'_1 = \frac{1}{h}\left(c_1 f_1 + c_2 f_2 + c_3 f_3 + c_4 f_4 + c_5 f_5 + c_6 f_6 + c_7 f_7 + c_8 f_8\right) \tag{25}$$

where

$$\begin{aligned}
c_1 &= -(\alpha_0 - 28\beta_0 + 13068)/5040 \\
c_2 &= +(\alpha_0 - 27\beta_0 + 5040)/720 \\
c_3 &= -(\alpha_0 - 26\beta_0 + 2520)/240 \\
c_4 &= +(\alpha_0 - 25\beta_0 + 1680)/144 \\
c_5 &= -(\alpha_0 - 24\beta_0 + 1260)/144 \\
c_6 &= +(\alpha_0 - 23\beta_0 + 1008)/240 \\
c_7 &= -(\alpha_0 - 22\beta_0 + 840)/720 \\
c_8 &= +(\alpha_0 - 21\beta_0 + 720)/5040,
\end{aligned} \tag{26}$$

$\alpha_0 = 1809.257$ and $\beta_0 = -65.1944$. For $i = 2$, the first derivative may be obtained from the following $O(h^5)$ approximation:

$$f'_2 = \frac{1}{h}\left(d_1 f_1 + d_2 f_2 + d_3 f_3 + d_4 f_4 + d_5 f_5 + d_6 f_6 + d_7 f_7 + d_8 f_8\right) \tag{27}$$

where

$$\begin{aligned} d_1 &= -(\alpha_1 - 21\beta_1 + 720)/5040 \\ d_2 &= +(\alpha_1 - 20\beta_1 - 1044)/720 \\ d_3 &= -(\alpha_1 - 19\beta_1 - 720)/240 \\ d_4 &= +(\alpha_1 - 18\beta_1 - 360)/144 \\ d_5 &= -(\alpha_1 - 17\beta_1 - 240)/144 \\ d_6 &= +(\alpha_1 - 16\beta_1 - 180)/240 \\ d_7 &= -(\alpha_1 - 15\beta_1 - 144)/720 \\ d_8 &= +(\alpha_1 - 14\beta_1 - 120)/5040 \end{aligned} \tag{28}$$

$\alpha_1 = -262.16$ and $\beta_1 = -26.6742$. Similar expressions for the first derivatives are defined at $i = N$ and $i = N + 1$. The stencils in (25)-(28) are analyzed in detail by Carpenter *et al.* (1993).

1.4.2 Second order derivative

For $i > 2$ and $i < N$, the second derivative of function $f(z)$ is computed using the following $O(h^6)$ approximation discussed by Lele (1992):

$$\frac{2}{11} f'_{i-1} + f'_i + \frac{2}{11} f'_{i+1} = \frac{1}{h^2} \left(\frac{3}{44} f_{i-2} + \frac{12}{11} f_{i-1} - \frac{51}{22} f_i + \frac{12}{11} f_{i+1} + \frac{3}{44} f_{i+2} \right). \tag{29}$$

For $i = 1$, the second derivative may be obtained from the following $O(h^5)$ approximation:

$$f''_1 = \frac{1}{h^2} \left(c_1 f_1 + c_2 f_2 + c_3 f_3 + c_4 f_4 + c_5 f_5 + c_6 f_6 + c_7 f_7 + c_8 f_8 \right) \tag{30}$$

where $c_1 = 5.211$, $c_2 = -22.300$, $c_3 = 43.950$, $c_4 = -52.722$, $c_5 = 41.000$, $c_6 = -20.100$, $c_7 = 5.661$, and $c_8 = -0.700$. For $i = 2$, the second derivative may be obtained from the following $O(h^5)$ approximation:

$$f''_2 = \frac{1}{h^2} \left(d_1 f_1 + d_2 f_2 + d_3 f_3 + d_4 f_4 + d_5 f_5 + d_6 f_6 + d_7 f_7 + d_8 f_8 \right) \tag{31}$$

where $d_1 = 0.700$, $d_2 = -0.389$, $d_3 = -2.700$, $d_4 = 4.750$, $d_5 = -3.722$, $d_6 = 1.800$, $d_7 = -0.500$, and $d_8 = 0.061$. Similar expressions for the second derivatives are defined at $i = N$ and $i = N + 1$. The stencils in (30) and (31) are courtesy of T. L. Jackson (University of Illinois at Urbana-Champaign, personal communication) and may be derived using a similar approach to that of Carpenter *et al.* (1993).

When solving the Poisson's equation for pressure in (20), the following alternate expressions are used (instead of (30)-(31)) leading to lower round-off errors. For $i = 1$

$$f_1'' = -\frac{1}{h}\frac{49}{10}f_1' + \frac{1}{h^2}\left(\frac{13489}{1800}f_1 + 12f_2 - \frac{15}{2}f_3 + \frac{40}{9}f_4 - \frac{15}{8}f_5 + \frac{12}{25}f_6 - \frac{1}{18}f_7\right) \tag{32}$$

with truncation error $0.6572h^6 d^8 f/dz^8$. Note that the Neumann pressure boundary condition in (20) is assigned through the first term in the right hand side of (32). For $i = 2$,

$$\begin{gathered}\frac{11}{128}f_{i-1}'' + f_i'' + \frac{11}{128}f_{i+1}'' = \\ \frac{1}{h^2}\left(\frac{585}{512}f_1 - \frac{141}{64}f_2 + \frac{459}{512}f_3 + \frac{9}{32}f_4 - \frac{85}{512}f_5 + \frac{3}{64}f_6 - \frac{3}{512}f_7\right)\end{gathered} \tag{33}$$

with truncation error $0.02101h^6 d^8 f/dz^8$. Similar expressions are used for $i = N + 1$ and $i = N$. The approximations in (32) and (33) and their corresponding truncation errors were derived via Taylor series analysis.

1.5 Grid-stretching

In order to resolve strong gradients in the x_3-direction near the bottom boundary and the top surface, a greater number of points is clustered near these two regions. Consider a set of equi-distant points at locations ξ_i discretizing the vertical direction of the domain. Clustering or stretching of these points may be accomplished through a mapping hyperbolic function (with existing real inverse) such as

$$z_i = (1/b)\,\tanh[\xi_i\,\tanh^{-1}(b)]. \tag{34}$$

This function takes the set of N equi-distant points ξ_i discretizing the interval $[-1, 1]$ and maps them to the set of N non-uniformly spaced points z_i in $[-1, 1]$. The points z_i are clustered near the upper and lower bounds of the interval. Coefficient b is a measure of the clustering.

The finite difference approximations of $\partial/\partial x_3$ and $\partial^2/\partial x_3^2$ used here (i.e. $\delta/\delta x_3$ and $\delta^2/\delta x_3^2$ can only be be applied over points which are equi-distant. Thus, derivatives on the non-uniform grid are computed in terms of derivatives on the equi-distant grid and derivatives of the inverse of the mapping function as

$$\frac{df}{dz} = \frac{df}{d\xi}\frac{d\xi}{dz} \quad \text{and} \quad \frac{d^2 f}{dz^2} = \frac{d^2 f}{d\xi^2}\left(\frac{d\xi}{dz}\right)^2 + \frac{df}{d\xi}\frac{d^2\xi}{dz^2}, \tag{35}$$

where z and ξ denote z_i and ξ_i, respectively, in (34). Note that this approach to clustering leads to non-uniformly spaced grid points in the vertical direction only. The grid points are uniformly spaced in the horizontal directions.

1.6 De-alisasing

The nonlinear advection term in (14) generates scales at high wavenumbers (i.e. small scales) unresolvable by the grid. This effect is reflected through an accumulation of energy

at the highest resolvable wavenumbers, often referred to as aliasing. In order to prevent this spurious accumulation, de-aliasing is performed using the well-known 3/2-rule in the horizontal directions. In the vertical direction, the high order (4th order) filter discussed by Slinn and Riley (1998) is used in order to attenuate the spurious high wavenumber energy accumulation while fully preserving the more energetic scales at lower wavenumber. Note that the subgrid-scale closures (the dynamic Smagorinsky and dynamic mixed subgrid-scale stress models) are nonlinear and can give rise to aliasing. However, the contribution of these closures is small and de-aliasing brings about a negligible change in results,

1.7 Spatial filtering of advection terms

As discussed earlier, the advection terms in the momentum equations are spatially filtered in the vertical direction in order to damp out scales of motion unresolvable by the grid. The following fourth order compact filter adapted for a non-uniform grid (Slinn and Riley, 1998) is used:

$$\begin{aligned} 0.4\tilde{f}_{i-1} + \tilde{f}_i + 0.4\tilde{f}_{i+1} &= 0.4f_{i-1} + f_i + 0.4f_{i+1} \\ &\quad -\frac{1}{80}(f_{i+2} - 4f_{i+1} + 6f_i - 4f_{i-1} + f_{i-2}) \\ &\quad -\frac{h}{80}\left(\frac{6\gamma_2(z_i)}{\gamma_1^2(z_i)}\right)\left(\frac{f_{i+2} - 2f_{i+1} + 2f_{i-1} - f_{i-2}}{2}\right) \\ &\quad -\frac{h^2}{80}\left(\frac{4\gamma_3(z_i)}{\gamma_1^3(z_i)} + \frac{3\gamma_2^2(z_i)}{\gamma_1^4(z_i)}\right)(f_{i+1} - 2f_i + u_{i-1}) \\ &\quad -\frac{h^3}{80}\left(\frac{\gamma_4(z_i)}{\gamma_1^4(z_i)}\right)\left(\frac{f_{i+1} - f_{i-1}}{2}\right) \end{aligned} \tag{36}$$

where $\gamma_1 = \partial\xi/\partial z$, $\gamma_2 = \partial^2\xi/\partial z^2$, $\gamma_3 = \partial^3\xi/\partial z^3$, and $\gamma_4 = \partial^4\xi/\partial z^4$ and ξ is the mapping function in (34). Note that this stencil is not valid for points at the bottom and top boundaries and for the first two horizontal planes of points off from these boundaries. In the current implementation the filter is not applied at these points. This omission does not have a negative impact on results.

A formal derivation of this compact filter can be made through Taylor series analysis. From this analysis one can see that the filtered function is an approximation of the unfiltered function up to 4th order. That is

$$\tilde{f} = f + O(h^4). \tag{37}$$

The finite difference approximations of the first and second derivatives in the vertical (x_3) direction (discussed in the previous subsection) introduce an error of $O(h^5)$ or higher. Filtering the advection terms in the vertical direction using (36) introduces an error of $O(h^4)$. Furthermore, using a spectral discretization in the horizontal (x_1 and x_2) directions introduces an error of much higher order than the previously discussed finite

differencing and filtering operations. Thus, the current spatial discretization is at least of $O(h^4)$. A higher order filter could potentially be introduced, however this would involve a more expensive computation at the expense of only minimally changing results.

2 Validation studies

Numerous simulations using the previously described method were carried out. The most rigorous were LES and direct numerical simulation (DNS) of turbulent channel flow between parallel walls at Re = 180. Looking at results such as mean velocity and resolved Reynolds stresses and one-dimensional spectra, LES performed with the current numerical method was more accurate than LES performed with lower order discretization methods, as expected.

2.1 Convergence results: Taylor-Green vortices and Poiseuille laminar channel flow

Temporal and spatial convergence results are presented in terms of two canonical problems, Taylor-Green vortices and Poiseuille laminar flow, respectively. The exact solution for the two-dimensional Taylor-Green vortices problem is

$$\begin{aligned} u_1(t,x_1,x_2,x_3) &= -\cos(x_1)\sin(x_3)\exp(-2\nu t) \\ u_2(t,x_1,x_2,x_3) &= 0 \\ u_3(t,x_1,x_2,x_3) &= \sin(x_1)\cos(x_3)\exp(-2\nu t) \\ p(t,x_1,x_2,x_3) &= \tfrac{1}{4}\left((\cos(2x_1)+\cos(2x_3)\right)\exp(-4\nu t) \end{aligned} \tag{38}$$

for $x_i \in [0, 2\pi]$. Periodicity is taken in x_1, x_2, and x_3 and the initial condition is prescribed as (38) with $t = 0$. A second version of this problem was also tested in a domain defined by $x_1 \in [0, 2\pi]$, $x_2 \in [0, 2\pi]$ and $x_3 \in [0, \pi]$ in which periodicity is taken in x_1 and x_2 and Dirichlet boundaries are taken at $x_3 = 0$ and $x_3 = \pi$. Figure (1a) clearly shows second order temporal convergence results for the latter problem on a $33\times9\times17$ grid. Other grids were tested leading to the same temporal convergence. Although these problems are relatively simple, they can quickly lead to the discovery of coding errors. Furthermore, through these problems we have confirmed the results of Kim and Moin (1985) and Armfield and Street (2000). That is, excluding the pressure gradient from the momentum solve in (19) or (16) leads to a first order time accurate method while retaining the pressure gradient leads to a second order time accurate method.

Figure (1b) shows spatial convergence results for a laminar Poiseuille channel flow. The exact solution is

$$\begin{aligned} u_1(t,x_1,x_2,x_3) &= u_{max}\left(1-\left(\frac{x_3}{h}\right)^2\right) \\ u_2(t,x_1,x_2,x_3) &= 0 \\ u_3(t,x_1,x_2,x_3) &= 0 \\ p(t,x_1,x_2,x_3) &= p_o - \frac{2u_{max}^2}{Re_h}\frac{x_1}{h} \end{aligned} \tag{39}$$

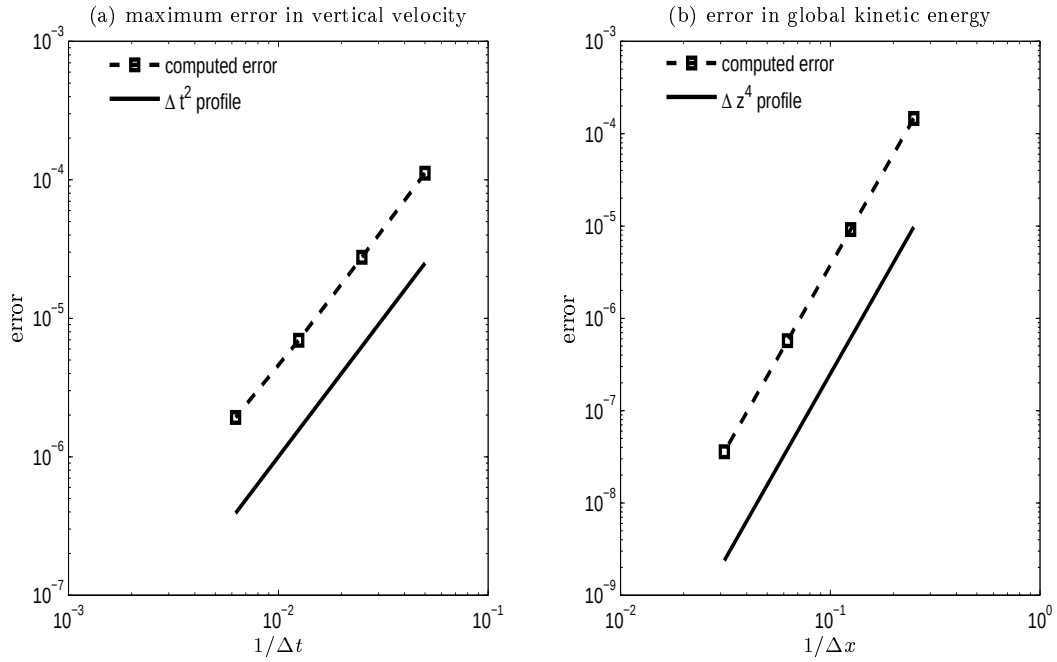

Figure 1: (a) Temporal convergence in Taylor-Green vortices problem and (b) spatial convergence in Poiseuille channel flow problem.

where h is the channel half-height, $Re_h = u_{max}h/\nu$ and u_{max} is the maximum centerline velocity. Note that the exact pressure solution in (39) is linear in x_1. However, the spectral discretization in x_1 and x_2 dictates that all solution variables must be periodic in these two directions. Thus, to have a periodic pressure we must take the pressure as a constant and account for the pressure gradient as a known forcing vector (F_1, F_2, F_3) on the right hand side of the momentum equation where $F_1 = 2u_{max}^2/Re_h$ and $F_2 = F_3 = 0$.

The initial condition is taken as $u_1 = (u_{max}/3)[1 - (x_3/h)^2]$, $u_2 = u_3 = p = 0$. Although this initial condition is not the exact solution, it is divergence-free. Furthermore, note that the exact solution to this problem is time-independent. Here the time splitting in the projection method serves as an iterator driving the numerical solution towards the exact, steady solution.

The spatial convergence result of Figure (1b) demonstrates that the spatial discretization employed is fourth order accurate, consistent with the fourth order spatial filter applied to the nonlinear advection term, discussed earlier.

2.2 Effects of grid cell size and subgrid-scale closure

This section presents studies exploring effects of grid cell size (or grid resolution) and subgrid-scale (SGS) closure on results of LES in flow with LC generated by intermediate waves with $\mathrm{La}_t = 0.7$. The effects of grid resolution and SGS closure are discussed in the same section because they are related to one another. As grid resolution is increased, the impact of the SGS closure weakens. Additionally, it is expected that effects due to grid resolution and subgrid-scale closure have a stronger impact on the LC flow at $\mathrm{Re} = 180$

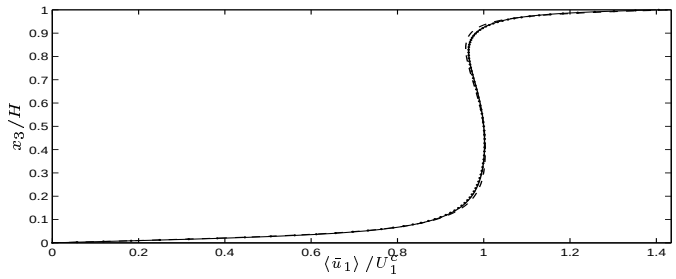

Figure 2: Profiles of mean velocity (normalized by U_1^c) for flows with LC at Re = 180 ($\lambda = 6H, \mathrm{La}_t = 0.7$) with different grid resolutions and subgrid-scale closures. ····· , simulation on $(32\times64\times97)$ grid with dynamic Smagorinsky closure; —— , simulation on $(48\times96\times145)$ grid with dynamic Smagorinsky closure; ---- , simulation on $(32\times64\times97)$ grid with dynamic mixed closure.

with the $(32 \times 64 \times 97)$ grid than on the LC flow at Re = 395 with the $(96 \times 96 \times 97)$ grid because of the coarser resolution in the former. Thus, results shown in this section were obtained with LC flow at Re = 180.

Simulation results obtained with the dynamic Smagorinsky closure and the dynamic mixed closure of Morinishi and Vasilyev (2001) are compared. In the latter closure, the deviatoric part of the SGS stress is computed as

$$\tau_{ij}^d = C_L(\bar{\bar{u}}_i\bar{\bar{u}}_j - \overline{\bar{u}_i\bar{u}_j})^d + 2(C_s\bar{\Delta})^2|\bar{S}|\bar{S}_{ij}. \tag{40}$$

In the former closure, τ_{ij}^d is given by (6). The coefficient $(C_s\bar{\Delta})^2$ in (40) is computed dynamically in the same way as before in (7). The coefficient C_L is computed dynamically as

$$C_L = \frac{\left\langle [L_{ij} + 2(C_s\bar{\Delta})^2 M_{ij}]H_{ij}^d \right\rangle}{\left\langle H_{kl}^d H_{kl}^d \right\rangle}, \tag{41}$$

where L_{ij} and M_{ij} are specified in (8) and (9), respectively, and

$$H_{ij} = (\widehat{\bar{\hat{u}}_i\bar{\hat{u}}_j} - \hat{\bar{\hat{u}}}_i\hat{\bar{\hat{u}}}_j) - (\widehat{\bar{u}_i\bar{u}_j} - \widehat{\bar{\bar{u}}_i\bar{\bar{u}}_j}). \tag{42}$$

Recall that the hat notation $\hat{\cdot}$, denotes application of a test filter over the horizontal directions of the flow. The bar notation, $\bar{\cdot}$, denotes application of the grid filter, implicitly set by the numerical method. Knowledge of the grid filter or at least an approximation to the grid filter is needed in order to compute the tensor H_{ij}. As an approximation to grid filtering, the following operation suggested by Morinishi and Vasilyev is used:

$$\bar{f}(x_i^*) = \frac{1}{24}[f(x_i^* - h_i) + 22f(x_i^*) + f(x_i^* + h_i)], \tag{43}$$

where $\bar{f}(x_i^*)$ is function f filtered over the x_i-direction evaluated at $x_i = x_i^*$ and h_i is the grid cell size in the x_i-direction. The width characterizing the filter induced by the operation in (43) is $\bar{\Delta}_i = h_i$. In the current implementation, the filter operation in (43) was applied over periodic directions of the flow (x_1 and x_2).

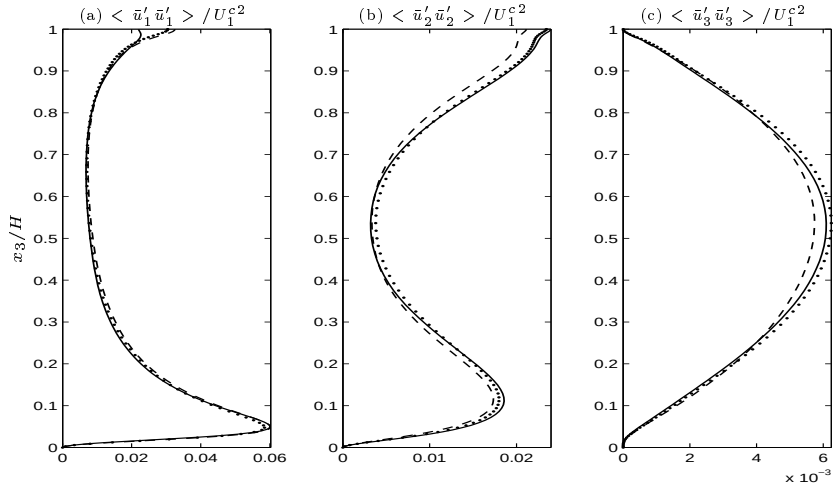

Figure 3: Resolved normal Reynolds stress components (normalized by U_1^{c2}) for flow with LC at Re = 180 ,($\lambda = 6H$, $\mathrm{La}_t = 0.7$) with different grid resolutions and subgrid-scale closures. ····· , simulation on $(32 \times 64 \times 97)$ grid with dynamic Smagorinsky closure; —— , simulation on $(48 \times 96 \times 145)$ grid with dynamic Smagorinsky closure; ---- , simulation on $(32 \times 64 \times 97)$ grid with dynamic mixed closure.

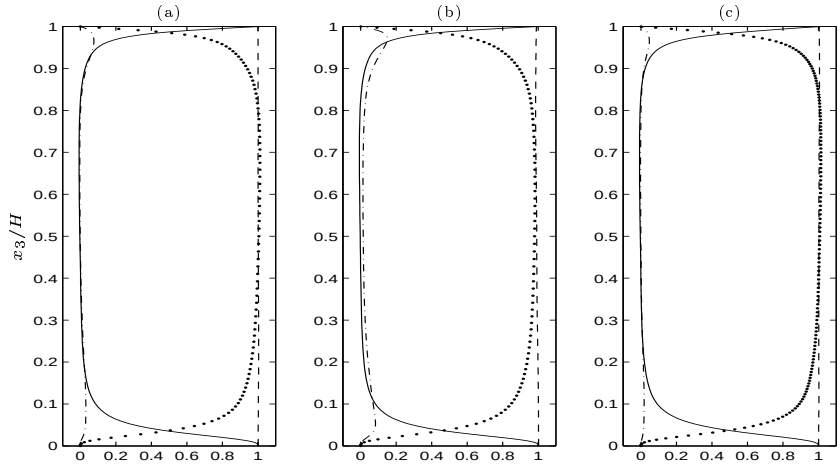

Figure 4: Mean dominant shear (1-3) component of resolved Reynolds stress, viscous stress and subgrid-scale stress for flows with LC Re = 180 ($\lambda = 6H, \mathrm{La}_t = 0.7$) with different grid resolutions and subgrid-scale closures. (a) Simulation on $(32 \times 64 \times 97)$ grid with dynamic Smagorinsky closure; (b) simulation on $(32 \times 64 \times 97)$ grid with dynamic mixed closure; (c) simulation on $(48 \times 96 \times 145)$ grid with dynamic Smagorinsky closure. ····· , 1-3 component of resolved Reynolds stress (i.e. $-\langle \bar{u}_1' \bar{u}_3' \rangle$); —— , 1-3 component of mean viscous stress (i.e. $(1/\mathrm{Re})\, d\langle \bar{u}_1 \rangle / dx_3$); —·— , 1-3 component of mean subgrid-scale stress (i.e. $< \tau_{13}^d >$); ---- , sum of previous three quantities. All quantities are normalized by the value of $< \tau_{13}^{\nu} >$ at the bottom wall (i.e. $< \tau_{13}^{\nu} > |_{x_3=0}$).

Before studying the effects of grid resolution and SGS closure, it is worthwhile to consider the Reynolds-averaged governing equations. Using the continuity equation, the viscous term in the momentum equation in (1) may be expressed as

$$\frac{1}{\mathrm{Re}}\frac{\partial^2 \bar{u}_i}{\partial x_j^2} = \frac{\partial \tau_{ij}^{\nu}}{\partial x_j}, \tag{44}$$

where the viscous stress is

$$\tau_{ij}^{\nu} = \frac{1}{\mathrm{Re}}\left(\frac{\partial \bar{u}_i}{\partial x_j} + \frac{\partial \bar{u}_j}{\partial x_i}\right). \tag{45}$$

Using the decomposition

$$\bar{u}_i = \langle \bar{u}_i \rangle + \bar{u}_i', \tag{46}$$

and equations (44) and (45), the x_1-momentum equation becomes

$$f(x_3) = -\frac{d\left\langle \bar{u}_1' \bar{u}_3' \right\rangle}{dx_3} + \frac{d\left\langle \tau_{13}^{d} \right\rangle}{dx_3} + \frac{d\left\langle \tau_{13}^{\nu} \right\rangle}{dx_3} = 0. \tag{47}$$

Integrating the previous expression in x_3 leads to

$$g(x_3) = -\left\langle \bar{u}_1' \bar{u}_3' \right\rangle + \left\langle \tau_{13}^{d} \right\rangle + \left\langle \tau_{13}^{\nu} \right\rangle = C, \tag{48}$$

where C is a constant. This constant can be determined by evaluating function $g(x_3)$ at the bottom wall (at $x_3 = 0$). At $x_3 = 0$, the 1-3 component of the resolved Reynolds stress tensor ($\langle \bar{u}_1' \bar{u}_3' \rangle$) and the 1-3 component of the subgrid-scale stress tensor (τ_{13}^{d}) both vanish. Thus, C is equal to the averaged 1-3 component of the viscous stress tensor at the bottom wall (i.e. $C = \langle \tau_{13}^{\nu} \rangle |_{x_3=0}$). Note that the 1-3 component of the subgrid-scale stress tensor and all of the other components of this tensor vanish at the bottom wall for both the dynamic Smagorinsky closure and the dynamic mixed closure. Now that C has been determined, expression (48) may be re-expressed as

$$\frac{g(x_3)}{\langle \tau_{13}^{\nu} \rangle |_{x_3=0}} = -\frac{\langle \bar{u}_1' \bar{u}_3' \rangle}{\langle \tau_{13}^{\nu} \rangle |_{x_3=0}} + \frac{\left\langle \tau_{13}^{d} \right\rangle}{\langle \tau_{13}^{\nu} \rangle |_{x_3=0}} + \frac{\langle \tau_{13}^{\nu} \rangle}{\langle \tau_{13}^{\nu} \rangle |_{x_3=0}} = 1. \tag{49}$$

Note that satisfaction of equation (47) serves as an indicator for turbulence under statistical equilibrium. For the flow configurations with and without LC, global conservation of streamwise momentum implies that the plane-averaged bottom stress should be equal to the prescribed surface stress (in the temporal mean). In all the cases presented in this article, temporal/plane averages of turbulent quantities were collected once the plane-averaged bottom stress normalized by τ_s was was close to one (in the temporal mean) throughout several flow-throughs. These averages were collected over a sufficiently long time period such that the relation in (47) was satisfied. Averaging over longer time periods resulted in nearly indistiguishable temporal/horizontal averages of turbulent quantities, thereby signaling that the turbulence had reached a statistical equilibrium.

Figures 2 and 3 compare mean streamwise velocity and resolved normal Reynolds stress components for three simulations all with LC generated by intermediate waves,

$\mathrm{La}_t = 0.7$ and $\mathrm{Re} = 180$. One of the simulations was performed with the dynamic Smagorinsky closure and another with the dynamic mixed closure, both on the $(32 \times 64 \times 97)$ grid with $b = 0.923$ discussed earlier. A third simulation was performed with the dynamic Smagorinsky closure but on a finer $(48 \times 96 \times 145)$ grid with $b = 0.859$. Mean streamwise velocity profiles (figure 2) are nearly indistinguishable in the three simulations. The simulations with equal resolution and different subgrid-scale closures predict values of $\langle \bar{u}_1' \bar{u}_1' \rangle$ very close to each other. In terms of $\langle \bar{u}_2' \bar{u}_2' \rangle$, the simulation with the dynamic mixed closure predicts slightly lower values especially in the upper and lower halves of the water column (figure 3b). In terms of $\langle \bar{u}_3' \bar{u}_3' \rangle$, the simulation with the dynamic mixed closure predicts slightly lower values, especially in the middle of the water column. These differences between the results with dynamic Smagorinsky and dynamic mixed closures are negligible. Most of the differences between the simulations with the dynamic Smagorinsky closure at different resolutions are negligible as well, thus verifying that the simulation on the coarser grid was not adversely affected by grid size. The main difference between the simulations with the dynamic Smagorinsky closure at different resolutions is in the predicted value of $\langle \bar{u}_1' \bar{u}_1' \rangle$ at the top surface. The simulation at coarser resolution overpredicts $\langle \bar{u}_1' \bar{u}_1' \rangle$ by about 10% relative to the simulation at finer resolution. This is attributable to the effect of the SGS closure which is greatest near the top surface. The impact of the SGS closure is greatly reduced with grid refinement, as will be shown next.

Figure 4 shows the dominant shear components (i.e. the 1-3 components) of resolved Reynolds stress, viscous stress and subgrid-scale stress in the three simulations previously discussed. In the simulation with the dynamic Smagorinsky closure, the 1-3 component of the subgrid-scale stress is given as $\tau_{13}^d = 2\nu_T \bar{S}_{13}$ where the eddy viscosity, ν_T, was defined in (6) and $\bar{S}_{13} = (\bar{u}_{1,3} + \bar{u}_{3,1})/2$. As discussed earlier, the presence of Langmuir circulations causes homogenization of the streamwise velocity in the middle of the water column. Consequently, the presence of the Langmuir circulations reduces the magnitude of $\bar{S}_{13}$ and thus of τ_{13}^d to nearly zero, especially in the middle third of the water column. This can be seen in Figure 4a. In the case of the dynamic mixed model, τ_{13}^d is not affected as much by homogenization of streamwise velocity because it is not solely proportional to $\bar{S}_{13}$ (see (40)). Looking at figures 4a-b, in the middle third of the water column, τ_{13}^d given by the dynamic mixed closure is greater than τ_{13}^d given by the dynamic Smagorinsky closure. In both simulations with the different subgrid-scale closures, the presence of Langmuir cells also tends to drive the 1-3 component of the mean viscous stress (i.e. $\langle \tau_{13}^\nu \rangle = \langle \bar{u}_{1,3} \rangle / \mathrm{Re}$) close to zero. Taking this into consideration together with the relation in (47), higher values of $\left\langle \tau_{13}^d \right\rangle$ lead to lower values of $-\langle \bar{u}_1' \bar{u}_3' \rangle$ when comparing the simulation with the dynamic mixed closure to its counterpart with the dynamic Smagorinsky closure. Note that for both of these simulations as well as for the simulation at greater resolution, the relation in (49) is well satisfied throughout the entire water column.

Comparing the simulations with the dynamic Smagorinsky closure at different resolutions (figures 4a,c), it can be seen that refining the grid leads to a reduction of $\left\langle \tau_{13}^d \right\rangle$, a well known attribute of the dynamic closure. This reduction is appreciable in regions near the bottom wall and near the top surface where values of $\left\langle \tau_{13}^d \right\rangle$ are larger than elsewhere.

2.3 Decaying isotropic turbulence

Under certain conditions, large-scale motions can become turbulent. More precisely, the large-scale motions become unstable and break into smaller scale motions which take energy from the larger ones. Energy is passed down to such small scales at which it is dissipated by the action of molecular viscosity. At high enough Reynolds numbers, the small-scale motions cease to depend on the nature of the large-scale flow, leading to universality of small-scale motions. Furthermore, these scales lose all directional orientation, thus becoming isotropic. The energy contained within these scales is characterized by what is usually referred to as the *five-thirds law*. In other words, the energy at these scales behaves as $k_r^{-5/3}$, where k_r, the radial wavenumber, is proportional the inverse of the size of the scales. Specifically, the radial wavenumber is defined as the magnitude of wavenumber $\mathbf{k}$.

In this section we present LES results with the dynamic Smagorinsky model of a flow which is nearly isotropic at all scales. Our results are compared to the experimental data of Comte-Bellot and Corrsin (1971), who represented an infinite space of isotropic motions decaying in time because of a lack of kinetic energy production (in the absence of shear flow) to balance the viscous dissipation. They accomplished this by obtaining a turbulent field behind a regular grid of bars spanning a steady, uniform duct flow. By moving at the speed of the mean flow behind the grid, they correctly surmised that an observer would see something like true isotropic turbulence evolving in time.

Due to the homogeneity of the flow, the domain is taken as a cube with sides of length 2π, and the boundary conditions are taken as periodic in the x_1-, x_2-, and x_3-directions. Furthermore, the cube is represented by a grid with 33 equally spaced vertices in each direction. Thus, the uniform spacing in all directions is $h = 2\pi/32$

Results are compared to the experimental data of Comte-Bellot and Corrsin (1971) in the form of energy spectra, or better yet, energy contained in the different scales of the flow. The initial condition for our simulations is obtained such that its energy spectrum matches filtered experimental spectrum at a particular non-dimensional time station of the Comte-Bellot and Corrsin experiment, denoted as t_{42}. The simulation is run for 56 time units up to a second non-dimensional time station, denoted as t_{98}, and the energy spectrum of the solution at this time is compared to the energy spectrum of the measured data corresponding to that same time station.

The solid curves in Figures (5a,b) show the energy spectrum of the initial condition in our simulation matching the energy spectrum of the Comte-Bellot and Corrsin (1971) experiment at t_{42}. The Reynolds number based on the Taylor microscale number of the initial condition is 137. The dashed curves show the energy spectrum of the solution in our simulation at t_{98}. Figures (5a,b) shows excellent agreement at t_{98} between the spectrum of the experiment (diamonds) and the spectrum of the simulation (dashed) for the smaller resolved scales in the range $5 < k_r h < 16$. The disagreement at lower wavenumbers is due to the limited length of the sides of the cubic domain.

Figure (5a) demonstrates the effect of explicit filtering in the x_3 (vertical) direction (analogous to de-aliasing in the x_1 and x_2 (horizontal) directions). Exclusion of either explicit filtering or de-aliasing (not shown) can lead to energy accumulation at high wavenumbers, as shown by the dash-dotted curves in Figure (5a).

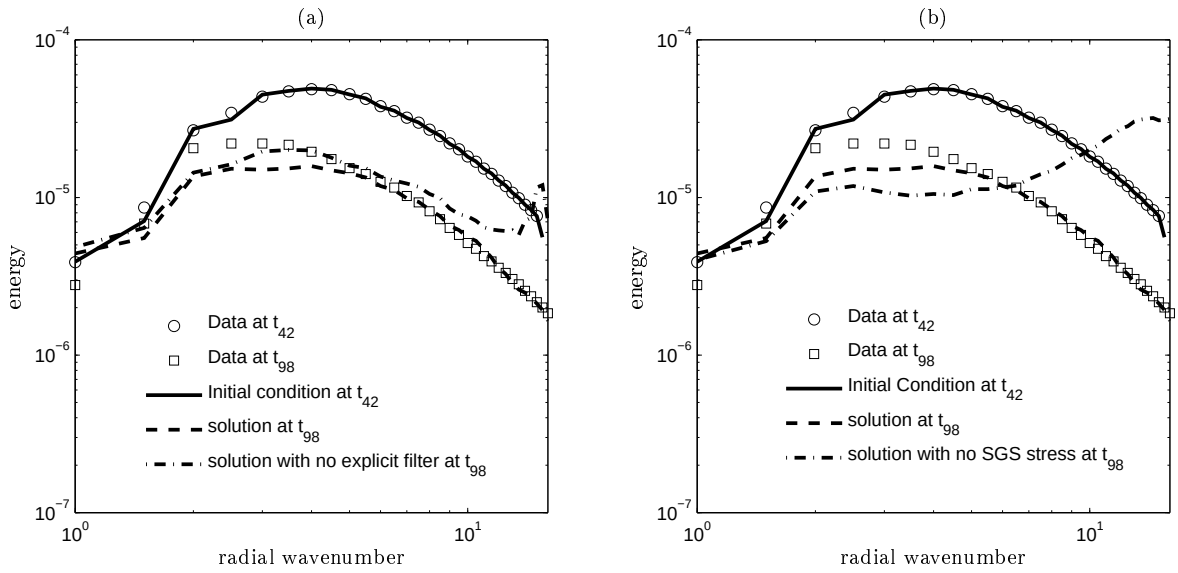

Figure 5: (a) Effect of explicit filtering on and, (b) effect of SGS stress model on advection terms in the x_3 direction in decaying isotropic turbulence.

Figure (5b) demonstrates the effect of the SGS parametrization, in this case the dynamic Smagorinsky model. The energy spectrum in the simulation without SGS parametrization is characterized by excessive energy accumulation for a large part of the resolved wavenumber range. The addition of the SGS parametrization leads to a drastic improvement as the SGS stress serves to extract energy from the resolved scales successfully modeling the effect of unresolved scales on resolved scales.

2.4 Turbulent channel flow

In this section we present DNS and dynamic Smagorinsky model LES results of unstratified turbulent channel flow between parallel, stationary, no-slip plates. The channel flow is chosen to have a Reynolds number, Re_τ, (based on the friction velocity, u_τ, and the channel half-height, h) at 180 for the purpose of comparison with the benchmark DNS results of Kim et al. (1987). The interested reader is directed to Tejada-Martínez et al. (2007) for recent results dealing with a stratified version of this flow. The friction velocity is defined as $u_\tau^2 = (\tau_w/\rho)$, where τ_w is the shear stress at the walls. By Dean's correlation, as given by Kim et al. (1987), $Re_\tau = 180$ corresponds to a bulk Reynolds number (based on the bulk streamwise velocity and channel half-height) of 2800. The geometry of the problem is composed of no-slip walls at $y = \pm h$ with homogeneous spanwise (x_2) and streamwise (x_1) directions. Thus, the spanwise and streamwise directions are taken as periodic. The channel domain is taken $L_1 = 4\pi h$ long the x_1 direction and $L_2 = (4/3)\pi h$ wide in the x_2 direction. The wall-normal direction extends from $x_3/h = -1$ to $x_3/h = 1$. The LES grid is composed of 33 points in the x_1 and x_2 directions and 65 points in the x_3 direction (i.e. $33 \times 33 \times 65$) while the DNS grid is composed of a $129 \times 129 \times 129$ grid. For our channel grid, a hyperbolic stretching function is employed in the wall-normal, x_3, direction such that the location of the first point off the top or bottom plate, x_3^*, is

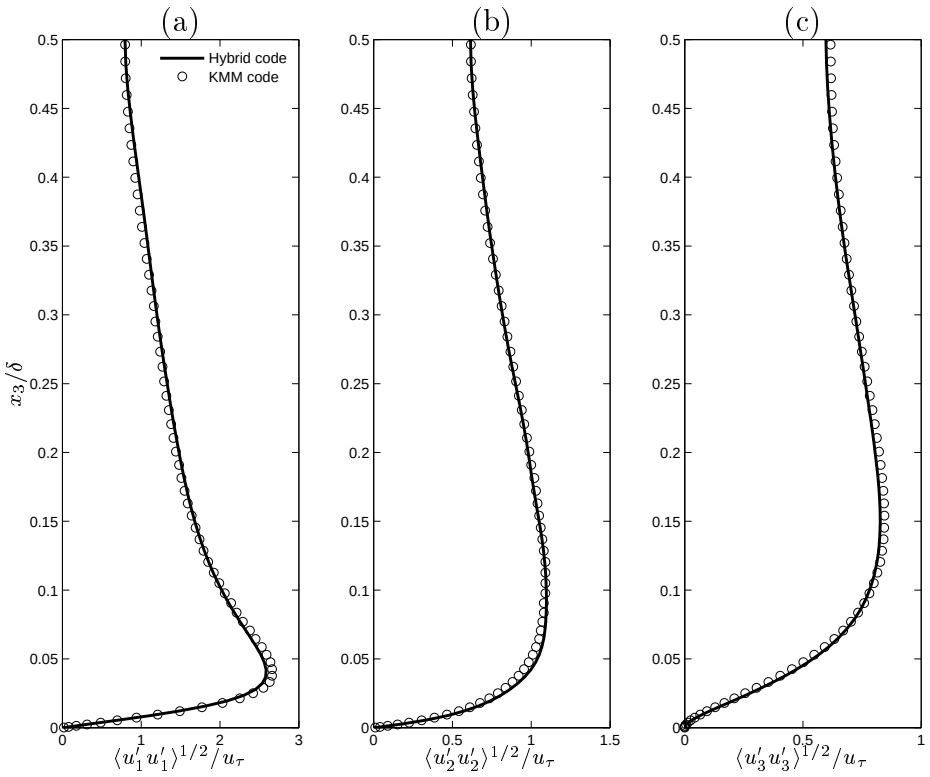

Figure 6: Root mean square of velocity fluctuations in DNS of turbulent channel flow.

set such that $\Delta z_1^+ = Re_\tau(\pm 1 - x_3^*) = 1$ for both DNS and LES. Using the stretching function, the grid spacings in the x_3 direction become smaller near the walls, yielding higher resolution in these regions. Due to the no-slip boundary conditions, a viscous boundary layer and its characteristic strong velocity gradient in the wall-normal direction develop in the near-wall region, requiring higher resolution in this region. The first point off the wall at $\Delta z_1^+ = 1$ is well below the top of the viscous boundary layer located at a $\Delta z^+ \sim 10$. Thus our LES may categorized as LES-NWR (i.e. LES with near-wall resolution).

In turbulent channel flow simulations, the flow is driven by a constant streamwise pressure gradient chosen such that (in a control volume setting) it balances the targeted wall shear stress determined by the choice of Re_τ. This balance results in the dimensionless streamwise pressure gradient equal to unity.

Figures (6a,b,c) and (7a,b) compare root mean square (rms) of velocity fluctuations, 1-3 Reynolds stress component and mean streamwise velocity, respectively, in our DNS of turbulent channel flow with the benchmark DNS of Kim et al. (1987). The rms of velocity fluctuations and the 1-3 Reynolds stress component are derived following the classical Reynolds decomposition:

$$\bar{u}_i = \langle \bar{u}_i \rangle + \bar{u}_i', \tag{50}$$

where $\langle \cdot \rangle$ denotes averaging in time and over homogenous directions (i.e. x_1 and x_2), $\langle \bar{u}_i \rangle$ is the mean velocity and $\bar{u}_i'$ is its fluctuating component. Based on this definition, the

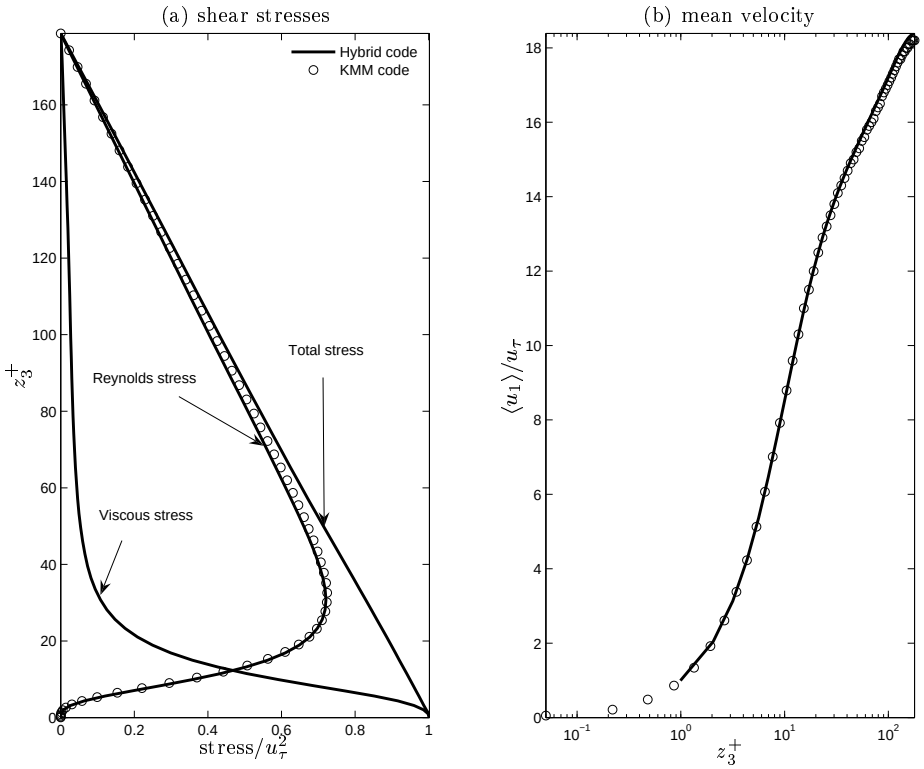

Figure 7: (a) Reynolds, viscous and total (Reynolds plus viscous) shear stresses and (b) mean velocity in wall units in DNS of turbulent channel flow.

Reynolds stress components are computed as $\langle \bar{u}_i' \bar{u}_j' \rangle = \langle \bar{u}_i \bar{u}_j \rangle - \langle \bar{u}_i \rangle \langle \bar{u}_j \rangle$ and the rms of velocity fluctuations as $u_1^{rms} = \sqrt{\langle \bar{u}_1'^2 \rangle}$, $u_2^{rms} = \sqrt{\langle \bar{u}_2'^2 \rangle}$ and $u_3^{rms} = \sqrt{\langle \bar{u}_3'^2 \rangle}$.

The agreement between the simulations in terms of rms of velocity fluctuations, 1-3 Reynolds stress component and mean streamwise velocity is remarkable given that our DNS was performed on a $129 \times 129 \times 129$ grid while the DNS of Kim et al. (1987) was performed on a much finer ($192 \times 160 \times 160$) grid. Figure (7a) also shows the 1-3 component of the viscous stress in our DNS. The sum of the 1-3 components of the viscous stress and Reynolds stress add up to a straight line as expected (Pope, 2000). Figure (7b) shows the mean velocity in wall units of our DNS as compared to that of Kim et al. (1987) on their finer grid. The agreement is excellent.

Figures (8), (9) and (10) show LES results in terms of the model coefficient, $(C_s \bar{\Delta})^2$ (appearing in the dynamic Smagorinsky SGS stress parametrization) and streamwise and spanwise energy spectra, respectively. Streamwise (spanwise) energy spectra is computed by taking the Fourier transform of streamwise (spanwise) autocorrelation functions. The two-point, one-time, streamwise correlation function is defined as

$$R_{ij}^x(\Delta x_1, x_3) = \frac{\left\langle \bar{u}_i'(t, x_1, x_2, x_3) \bar{u}_j'(t, x_1 + \Delta x_1, x_2, x_3) \right\rangle_{tx_2}}{\left\langle \bar{u}_i' \bar{u}_j' \right\rangle}. \tag{51}$$

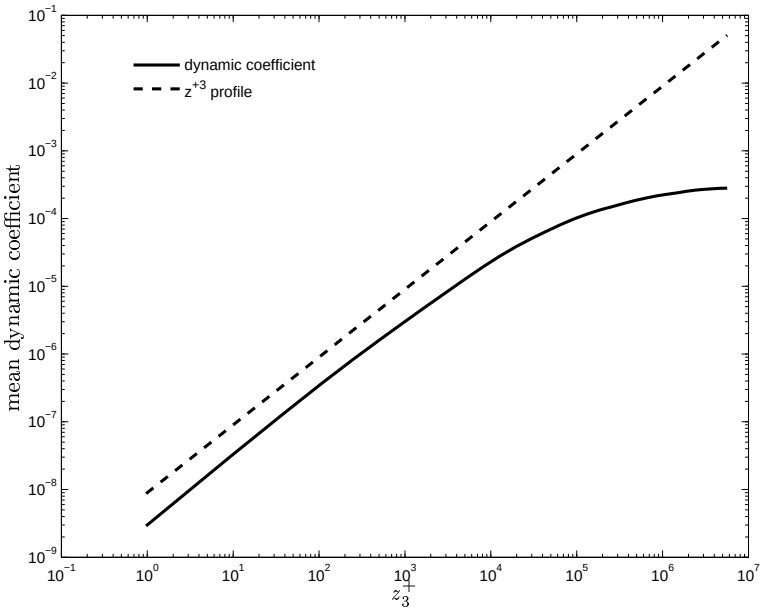

Figure 8: Mean dynamic coefficient, $< C_s^2 \Delta^2 >$, in LES of turbulent channel flow.

Similarly, the spanwise correlation function is

$$R_{ij}^{y}(\Delta x_2, x_3) = \frac{\left\langle \bar{u}_i'(t, x_1, x_2, x_3) \bar{u}_j'(t, x_1, x_2 + \Delta x_2, x_3) \right\rangle_{tx_1}}{\left\langle \bar{u}_i' \bar{u}_j' \right\rangle}, \tag{52}$$

where $\langle \cdot \rangle_{tx_i}$ denotes averaging in time and over the x_i-direction. Autocorrelations are obtained by setting $i = j$ in (51) and (52) and ignoring the usual convention of summing over repeated indices.

Near the wall, $(C_s \bar{\Delta})^2$ goes to zero as can be seen by analyzing equations (7), (8) and (9). More specifically, as expected, near the wall $(C_s \bar{\Delta})^2 \sim z^{+3} = (Re_\tau z)^3$ where z is the dimensionless distance to the wall (Pope, 2000). Streamwise and spanwise energy spectra at the middle horizontal plane and a near-wall horizontal plane of the channel from our LES compared to those from the DNS of Kim et al. (1987) demonstrates that the LES is able to accurately represent the energy in the most energetic scales of the flow. As expected, there is small damping of energy in the LES relative to the DNS at the highest resolved wavenumbers of the LES. This damping is due to an unknown combination of the spatiotemporal discretization and the SGS discretization. Note that the high wavenumber energy damping observed in LES with our high order spatial discretization is much less that the damping observed in LES with lower order methods. For comparison, the reader is directed to the LES results of Najjar and Tafti (1998) obtained with a second order accurate spatial discretization. In the latter, excessive streamwise energy damping occurs at $k_1 h \approx 10$. Finally, the reader is reminded that it is not possible to compare our LES energy spectra at exactly the same near-wall locations as those of Kim et al. (1987) due to different grids between our LES and their DNS. As a result, LES energy spectra in terms of wall-normal fluctuations at $z^+ = 4.75$ is lower than the DNS counterpart at $z^+ = 5.34$ for all wavenumbers resolved in the LES.

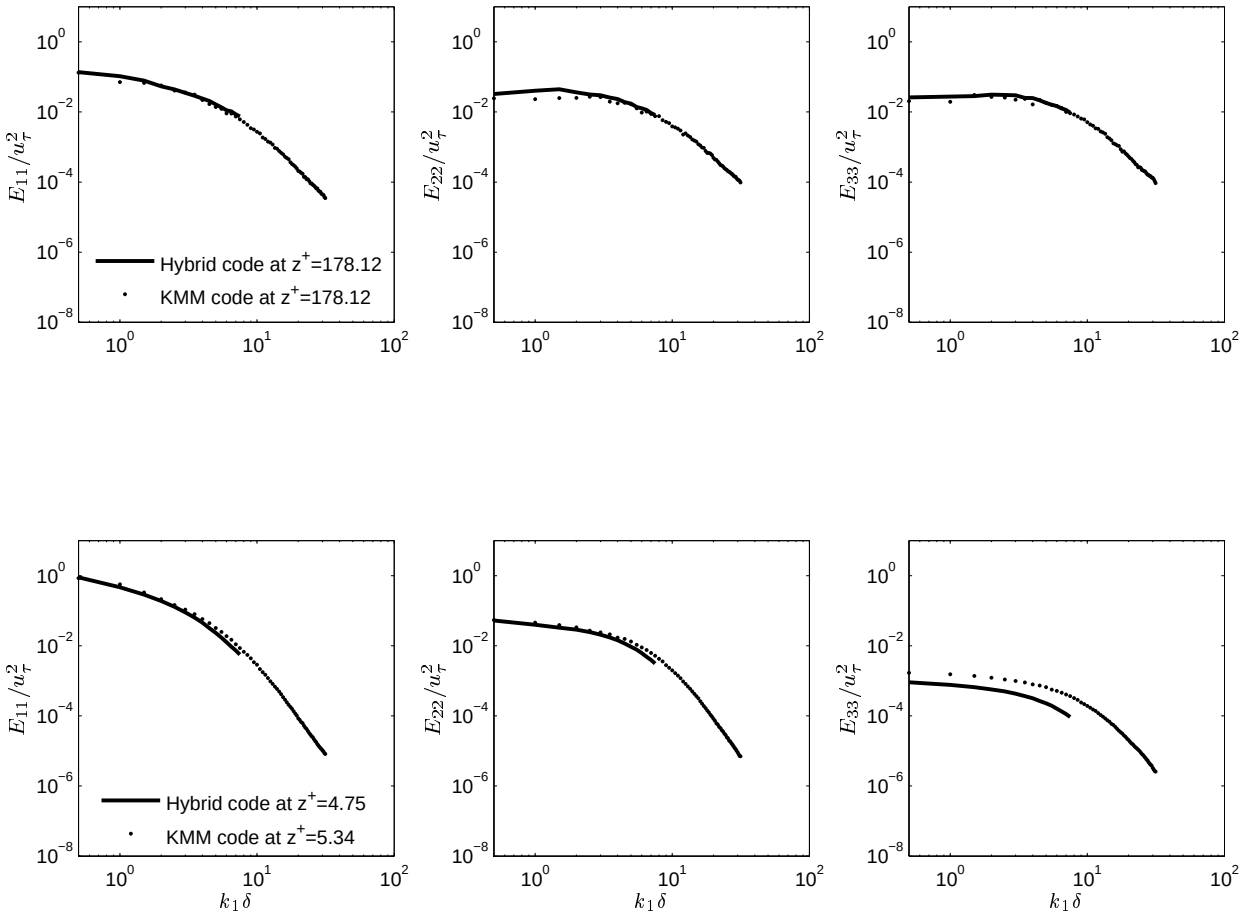

Figure 9: Streamwise one-dimensional energy spectra in LES of turbulent channel flow.

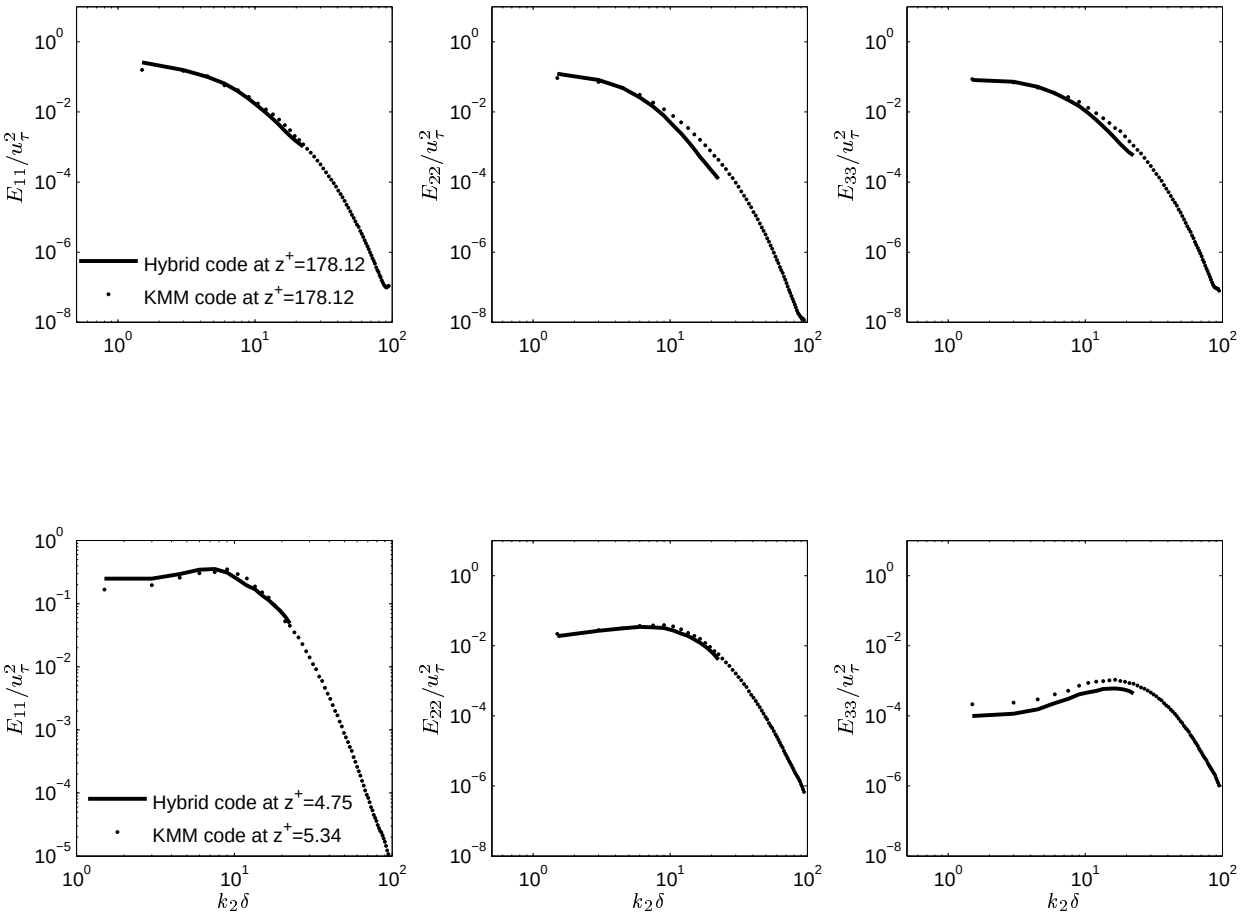

Figure 10: Spanwise one-dimensional energy spectra in LES of turbulent channel flow.